nature materials

ARTICLES

https://doi.org/10.1038/s41563-019-0598-7

Molecular understanding of charge storage and charging dynamics in supercapacitors with MOF electrodes and ionic liquid electrolytes

Sheng Bi[1,2], Harish Banda[3], Ming Chen[1,4], Liang Niu[1], Mingyu Chen[1], Taizheng Wu[1], Jiasheng Wang[1], Runxi Wang[1], Jiamao Feng[1], Tianyang Chen[3], Mircea Dincă[3], Alexei A. Kornyshev[2*] and Guang Feng[1*]

We performed constant-potential molecular dynamics simulations to analyse the double-layer structure and capacitive performance of supercapacitors composed of conductive metal–organic framework (MOF) electrodes and ionic liquids. The molecular modelling clarifies how ions transport and reside inside polarized porous MOFs, and then predicts the corresponding potential-dependent capacitance in characteristic shapes. The transmission line model was adopted to characterize the charging dynamics, which further allowed evaluation of the capacitive performance of this class of supercapacitors at the macroscale from the simulation-obtained data at the nanoscale. These 'computational microscopy' results were supported by macroscopic electrochemical measurements. Such a combined nanoscale-to-macroscale investigation demonstrates the potential of MOF supercapacitors for achieving unprecedentedly high volumetric energy and power densities. It gives molecular insights into preferred structures of MOFs for accomplishing consistent performance with optimal energy–power balance, providing a blueprint for future characterization and design of these new supercapacitor systems.

Enhancing the capacitive performance of electrical double-layer capacitors (EDLCs) relies on the development of porous electrode materials[1,2]. Owing to their designable structures[3–5], conductive metal–organic frameworks (MOFs) are promising for EDLC electrodes[5–8]. Their scaffold-shaped volume-filling ordered structure could provide large specific surface area (SSA) per mass/volume, with a custom-designed pore space[3,6]. This helps to maximize the stored energy density; it may also facilitate ion transport, thereby increasing power density. Indeed, graphene-doped MOFs were found to have high capacitance, due to their high porosity and open structure[9]. Highly conductive Ni_3(2,3,6,7,10,11-hexaiminotriphenylene)$_2$ ($Ni_3(HITP)_2$) MOF electrodes in EDLCs with an organic electrolyte showed high areal capacitance and low cell resistance, superior to most carbon-based materials[10].

The choice of electrolyte is equally important. Room-temperature ionic liquids (RTILs) are promising electrolytes due to their excellent thermal stability, non-volatility, broad working temperature range and wide electrochemical window (potentially facilitating the EDLC's energy density)[11–14]. Many studies have focused on understanding the energy storage mechanism of porous electrodes with RTILs, via in situ experiments and molecular simulations[11,15–18]. Traditional electrodes, for example activated carbons, contain pores of different sizes, shapes and connectivities[1,2], whereas MOFs present monodisperse pores with controllable structures[3–5,7], making them near-ideal systems for computational modelling. Nevertheless, because there could be millions of MOF–RTIL combinations, it is important to clarify generic charge storage mechanisms and charging dynamics related to their structures, particularly in the absence of experimental studies on supercapacitors with conductive MOF electrodes and RTIL electrolytes.

Herein we focus on this task, using 'computational microscopy'—molecular dynamics (MD) simulations based on atomistic models of MOFs and coarse-grained models of RTILs—and connecting with 'experimental macroscopy'—electrochemical measurements on MOF–RTIL supercapacitors. Figure 1a shows our MD set-up; we consider three types of electrodes based on densely stacked two-dimensional (2D) conductive MOF sheets with different-sized quasi-one-dimensional (1D) pores (Fig. 1b,c), and 1-ethyl-3-methylimidazolium tetrafluoroborate ([EMIM][BF_4]) as the electrolyte (Fig. 1d). In simulations, we control the voltage between cathode and anode by the constant-potential method. For details see Methods and Supplementary Sections 1 and 2. After equilibrating the system at the potential of zero charge (PZC), we apply jump-wise voltages between two electrodes, and then monitor the follow-up charging dynamics and charge/ion distributions. We explore structures of ionic distributions in electrically polarized nanoscale pores, and the options for energy storage and power delivery that these structures proffer. Finally, we experimentally test the simulation-predicted performance.

Equilibrium charge and ion distributions inside MOFs

We present the simulated charge and ion distributions in three neutral and polarized MOFs with pore sizes of 0.81, 1.57 and 2.39 nm, and PZCs calculated as 0.074, 0.035 and 0.042 V, respectively. The small PZC values suggest no noticeable preferential adsorption of cations or anions of [EMIM][BF_4] into the pores of these MOFs[19].

Figure 2a depicts the in-plane distributions in a 1.57-nm-diameter pore at different electrode potentials. Inside quasi-1D pores of a polarized MOF electrode, radial ion distributions appear more heterogeneous than those at the PZC, with counter-charge settling

[1]State Key Laboratory of Coal Combustion, School of Energy and Power Engineering, Huazhong University of Science and Technology (HUST), Wuhan, China. [2]Department of Chemistry, Faculty of Natural Sciences, Imperial College London, London, UK. [3]Department of Chemistry, Massachusetts Institute of Technology, Cambridge, MA, USA. [4]Shenzhen Research Institute of HUST, Shenzhen, China. *e-mail: a.kornyshev@imperial.ac.uk; gfeng@hust.edu.cn

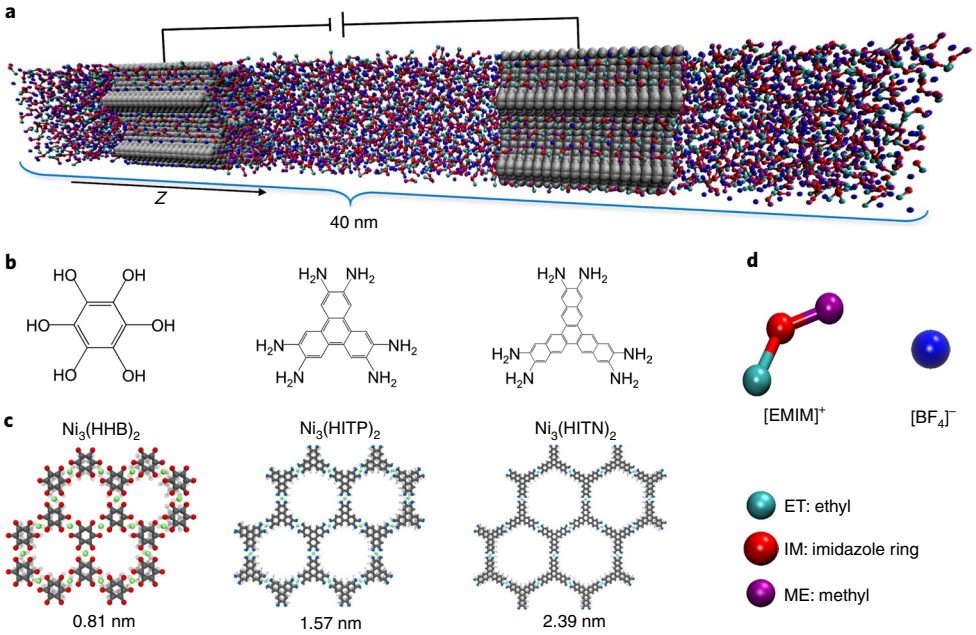

Fig. 1 | Schematics of molecular simulations of MOF-based supercapacitors. a, A snapshot of the simulation system containing two identical MOF electrodes connected with RTIL reservoirs (periodically repeated in all three dimensions). Each electrode has stacks of 18 2D MOF sheets. **b**, Molecular structures of the linkers used for three studied MOFs. **c**, 2D honeycomb structures of studied MOF sheets. The numbers at the bottom indicate characteristic in-plane sizes of quasi-1D pores formed by the stacked MOF sheets (that is, effective pore diameters). **d**, Coarse-grained model of the RTIL [EMIM][BF_4]. Details for all three studied MOFs and the simulation set-up can be found in Supplementary Section 1 and Supplementary Tables 1–3.

closer to the pore surface and at the pore centre-line (top row of Fig. 2a). At the PZC, as shown in the middle and bottom rows of Fig. 2a, cations and anions both form a layer adsorbed on the pore surface, displaying a hexagonal pattern in the planar cross-section, with a wire of ions along the pore axis. Under electrode polarization, the counter-ions (cations at negative and anions at positive polarization) pack similarly but with more distinct separation between a surface-adsorbed layer and the centre-line. The co-ions settle between these two regions. For the smallest pore MOF (0.81 nm), only one layer (a single column) of ions can get inside the pore, regardless of electrode polarization (Supplementary Fig. 5). For the largest pore (2.39 nm), at the PZC, two mixed cation–anion layers dwell inside the pore, one of them contacting the pore wall; under electrode polarization two pronounced counter-ion layers form, separated by a co-ion layer, with a co-ion wire at the axis (Supplementary Fig. 6).

The interlaced radial distributions of cations and anions in polarized pores comply with the ion layering in RTILs at electrode surfaces revealed by previous experiments and simulations[11,15–17], while there is little cation–anion layering at the PZC (middle column of Fig. 2a). To delve into this difference, we analysed the ion density along the pore axis. In Supplementary Fig. 7a we see that waving axial ion distributions at PZC become more distinct with electrode polarization. Examining ions inside pores, we divided the pore space into central and surface regions demarcated by a circle with radius of 0.25 nm (Fig. 2b and snapshots in Supplementary Fig. 7b). The cation orientations, characterized by angular distributions (Fig. 2c), reveal how ions are accommodated inside the pore. As the electrode becomes more negatively charged, cations in the surface region prefer to align along the pore axis, while those in the central region orientate more randomly, which could be ascribed to the adsorbed ion layer screening out the electrode surface charge. With positive polarization, the cations move closer to the centre axis and leave their ethyl groups pointing to surface-adsorbed anions. Similar trends could be observed for smaller and larger pores (Supplementary Figs. 8 and 9), except that ions in the central region of larger pores orientate more randomly. The delineated in-plane and axial ion distributions clarify where and why ions could preferably reside in MOF pores[11,15,20].

Capacitance and energy density of MOF-based supercapacitors

Charge storage in supercapacitors is characterized by voltage-dependent capacitance and energy density. The differential capacitance of an electrode is defined as the derivative of the electrode's charge with respect to its potential (Methods and Supplementary Section 2). The electrode charge is of equal magnitude and opposite sign to the net ionic charge inside the pores and in the double layer at the electrode's outer surface. For highly porous electrodes, the area of the latter is negligible, and we will not consider this contribution.

The capacitance is usually presented per unit (1) surface area (area specific), (2) mass (gravimetric) or (3) volume (volumetric) of the electrode. The gravimetric and volumetric values are easy to define, whereas the determination of the area-specific capacitance could be ambiguous, as it depends on how the interior surface of the electrode was measured (the way we estimated the surface area of the studied MOF pores is described in Supplementary Section 1). Figure 3a shows the area-specific differential capacitance. The MOF with the smallest pore (0.81 nm) displays a double-humped shape of the capacitance–potential curve with two maxima of 10.2 and 8.8 μF cm^{-2} at −1.1 and +1.5 V, respectively, while the curves for the other two MOFs are both bell shaped with a maximum near the PZC. Within a potential range of −0.5 to +0.5 V, the 1.57-nm-diameter MOF delivers a capacitance of ~9 μF cm^{-2}, compatible with RTIL-based porous carbon EDLCs[17,21]. The shape of the capacitance–potential curves could be understood through analysing the voltage-dependent ion distributions inside pores (Supplementary Fig. 10). There, for the smallest pore MOF, the numbers of in-pore cations and anions, separately, gradually change within the potential range between −1 and +1.4 V (Supplementary Fig. 10a).

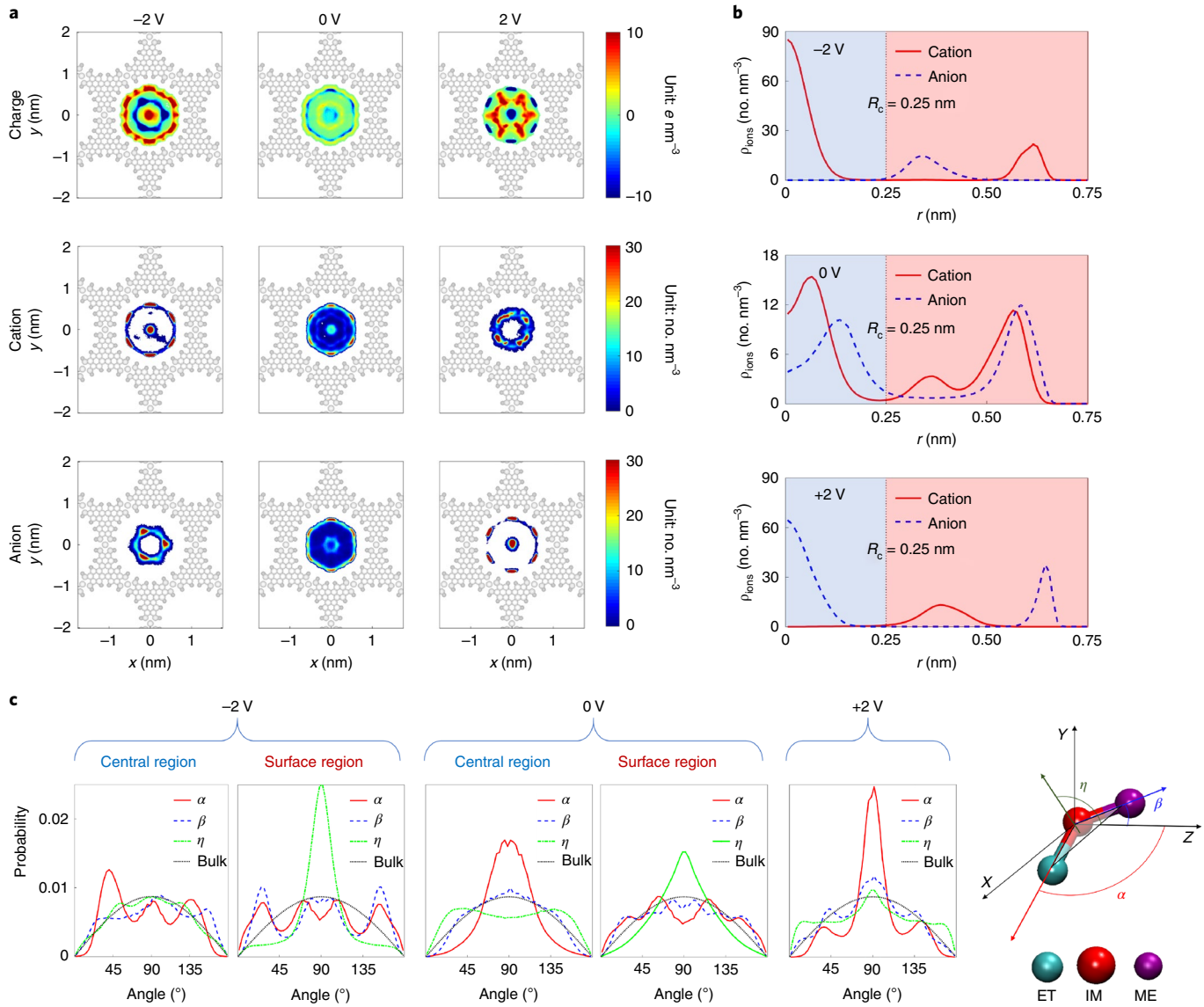

Fig. 2 | In-pore charge/ion density and orientation distributions. a, In-plane, 2D maps of charge and ion distributions of [EMIM][BF_4] inside pores of a studied MOF. Each map is based on simulation data averaged along the pore axis (the pore diameter is 1.57 nm). Columns correspond to three (indicated) electrode potentials (0 V means PZC, see main text) and rows indicate 2D charge distributions and 2D number density distributions of cations and anions. For better visibility, results for neighbouring pores are not displayed, and in the central pore the areas where no ions could access are shown in white. **b**, Radial number distributions of ions inside the pore. $r = 0$ stands for the pore centre. The light-blue and red shaded areas, separated by a critical value of radial distance ($R_c = 0.25$ nm), represent the central and surface regions of the pore space. **c**, Angular distribution of cations located in central and surface regions of the MOF pore.

The change becomes faster under larger electrode polarizations, slowing down after ±2 V, approaching saturation. This results in the double-humped shape of the capacitance–potential curve (Fig. 3a). For the other two MOFs (Supplementary Fig. 10b,c), the steepest change in ion population occurs near the PZC, slowing down as the electrodes become more polarized (especially above ±1.5 V); this induces bell-shaped capacitance–potential curves (Fig. 3a). Notably, for pores filled with more than one ion layer, within the potential range of −0.5 to +0.5 V the change of cation/anion population takes place mainly in the central region of a pore, but it shifts towards the pore surface region beyond this range (Supplementary Fig. 10d,e).

Having defined the mass and volume of a unit cell for the studied MOFs, we obtain the gravimetric/volumetric capacitances, and the corresponding energy densities. As shown in Fig. 3b,c, the MOF with the largest pore (2.39 nm) has the highest gravimetric capacitance but the lowest volumetric one. For the 1.57-nm $Ni_3(HITP)_2$ MOF, the gravimetric and volumetric capacitances reach 112 F g^{-1} and 105 F cm^{-3}, respectively. Notably, simulations show that a gravimetric energy density of ~57 Wh kg^{-1} could be achieved at a cell voltage of 4 V, if the electrodes could sustain this voltage. Such energy density is as high as those reported for some high-energy-density carbon electrodes[22]. With regards to volumetric energy density, especially within a narrower potential range, the three MOF electrodes display similar capacitances, while at a cell voltage of 4 V the smallest-pore MOF delivers the highest volumetric energy density, ~50 Wh l^{-1}. The predicted volumetric performance demonstrates promising potential of these MOFs in comparison with other electrode materials in EDLCs[23,24].

Certainly, as the pore size of MOFs keeps reducing, ions eventually will not be able to enter the pores, leading to vanishing

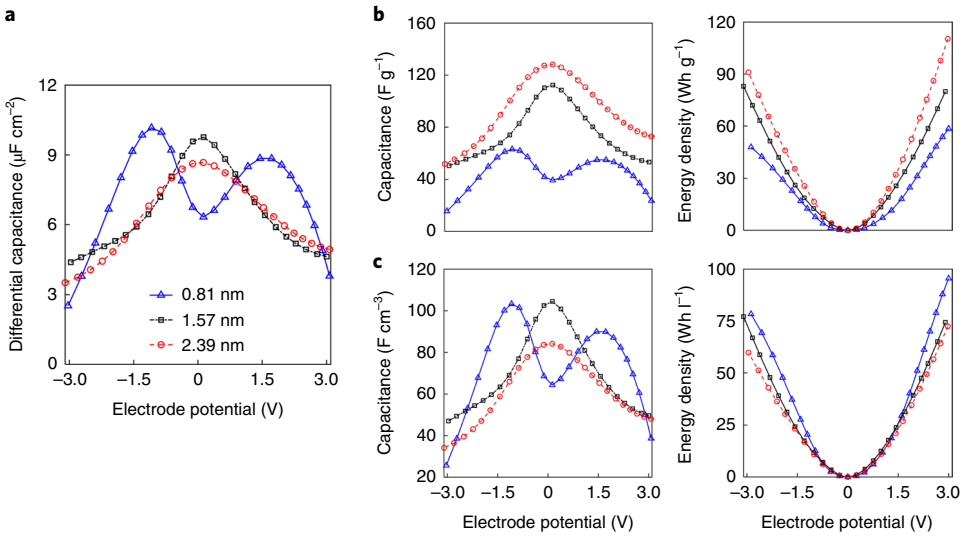

Fig. 3 | Capacitance and energy density. Voltage dependence of the capacitance and stored energy density of an ionic-liquid-filled MOF electrode. **a**, Differential capacitance per unit pore surface area. **b**,**c**, Gravimetric (**b**) and volumetric (**c**) capacitance and energy density of the three studied MOFs. The energy density is calculated from $E_{g/v}(\Phi) = \int_{PZC}^{\Phi} \phi C_{g/v}(\phi)\, d\phi$, where $C_{g/v}$ is the gravimetric/volumetric capacitance and Φ is the electrode potential.

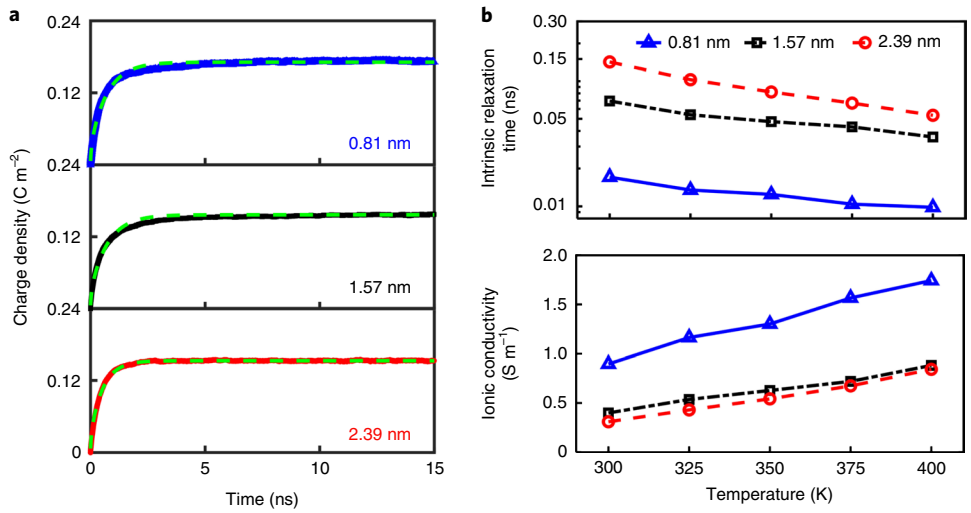

Fig. 4 | Charging process at nanoscale. a, Time evolution of charge density per unit surface area of the pore, after a cell voltage of 4 V was applied between two electrodes, shown for the positive electrode, for the three MOFs of indicated pore sizes at 400 K. Simulation-obtained results are shown against the curves (green dashed lines) fitted by the TLM sketched in Supplementary Fig. 14a. **b**, Intrinsic relaxation time (top panel, shown in logarithmic scale for better visibility) and ionic conductivity (bottom panel) of RTILs in the MOF pores at different temperatures.

capacitance. Indeed, the Ni_3(hexaaminobenzene)$_2$ ($Ni_3(HAB)_2$) MOF[8], with rather less room than $Ni_3(HHB)_2$ to accommodate enough ions inside, was found to exhibit considerably smaller capacitance, suggesting that there would be a limit of narrowing MOF pore for a typical RTIL (Supplementary Figs. 11 and 12 in Supplementary Section 4).

Charging dynamics

We focus now on power delivery. Figure 4a shows the time evolution of ionic charge in a pore at 400 K (for results between 300 and 400 K, see Supplementary Fig. 13). It appears possible to rationalize the charging dynamics through the transmission line model (TLM)[25]. On the basis of the TLM schematized in Supplementary Fig. 14a, the net charge of the pore, after jump-wise application of a constant potential, reads[25]

$$Q(t) = Q_\infty \left\{ 1 - \frac{2}{\pi^2} \sum_{n=0}^{\infty} \frac{\exp\left[-\pi^2 \left(n+\frac{1}{2}\right)^2 \left(\frac{2\ell}{L}\right)^2 \frac{t}{\tau} \right]}{\left(n+\frac{1}{2}\right)^2} \right\} \qquad (1)$$

where Q_∞ is the charge when the pore is fully charged, l is the pore volume divided by its surface area and L is the full length of the pore. The parameter in equation (1), which does not depend on pore length, is the intrinsic relaxation time,

$$\tau = \frac{C_{area} l}{\sigma} \qquad (2)$$

in which C_{area} is the areal capacitance of the pore and σ is the ionic conductivity inside the pore. Note that equation (1) is strictly valid for potential-independent capacitance; there is no closed-form solution if the capacitance varies during charging. For simplicity, we

will still use equations (1) and (2) with the value of C_{area} corresponding to the capacitance for a given electrode potential.

Taking the 1.57-nm-diameter MOF, with $l = 0.40$ nm and $L = 5.86$ nm (for parameters for the other two MOFs, see Supplementary Tables 2 and 3), by fitting TLM to simulation data we obtain τ. Despite the aforementioned approximation, TLM-fitted curves match the MD-obtained charging curves very well (see Fig. 4a). This is further confirmed by fittings of the charging dynamics under alternative voltage jumps and at different temperatures (Supplementary Figs. 13 and 14b–d). The fittings for all three studied MOFs show that with increasing temperature τ decreases (top panel of Fig. 4b), which is reasonable and has been experimentally demonstrated for porous electrodes owing to the increase of ion mobility with increasing temperature[26,27]. The obtained value of τ can be used to roughly estimate the charging time, $\tau_0 = \frac{\tau}{(l/L)^2}$, for a practical supercapacitor cell. For instance, for a 1.57-nm-pore MOF electrode of 100 μm thickness, τ_0 will be about 4.3 and 2.2 s at 300 and 400 K, respectively.

Specially performed MD simulations of bulk [EMIM][BF_4] give a conductivity of 1.26–8.2 S m^{-1} within 300–400 K, consistent with experimental data (1.6–10.8 S m^{-1}) (ref. [28]). To evaluate the conductivity of in-pore RTIL, we extracted the values of τ from fitting equation (1) to the MD-obtained charging curves in Fig. 4a, and then find σ, using equation (2). For MOFs with pore sizes of 1.57 and 2.39 nm, σ increases from 0.3 to 0.9 S m^{-1} within 300–400 K (bottom panel of Fig. 4b). Interestingly, the conductivity of ions in the smallest pore (0.81 nm), varying in the range of 0.9–1.7 S m^{-1} in this temperature interval, appears higher than in the other two larger MOF pores. This could be attributed to the stronger screening electrostatic interactions due to the induced image charges on the pore walls[29,30]. Nevertheless, the conductivities of ions under nanoconfinement are obviously smaller than in the bulk.

These results suggest considerable limitations for ion transport inside the quasi-1D MOF pores. Hence, the electrolyte resistance in MOFs would be the dominant contribution to the equivalent series resistance (ESR) of a practical MOF-based EDLC. This is similar to what has been concluded from the experiment with a 1.57-nm-pore MOF in an organic solution[10]. It is simply because the electrical conductivity of this MOF is much higher than the ionic conductivity of the in-pore RTIL. Interestingly, the higher working voltage results in a decrease of τ and an increase of σ (Supplementary Fig. 14e–g), thus promoting faster ion transport inside the MOFs.

All the above simulations are conducted with the RTIL in a coarse-grained model[31] and the MOF electrode in AA interlayer stacking[32]. To verify the independence of the ion model from results, we employed an all-atom model for [EMIM][BF_4] (Supplementary Fig. 15)[33]. The all-atom model gave results very similar to the coarse-grained one, including in-pore ion distributions, charge storage and charging dynamics (Supplementary Figs. 16–18). To reveal the effect of interlayer stacking, we performed MD simulations on a slipped-parallel AB stacking model[32] of the $Ni_3(HITP)_2$ MOF (Supplementary Fig. 19a). The tiny parallel slip (0.137 nm) introduces a negligible difference in both capacitance and charging dynamics (Supplementary Fig. 19b).

Capacitive performance at the macroscale

To validate the MD-obtained capacitance, taking the $Ni_3(HITP)_2$ MOF as an example, we carried out electrochemical measurements of supercapacitors with [EMIM][BF_4] electrolyte. We have set up three synthesis procedures (Methods), based on previously reported strategies[10,34], and obtained $Ni_3(HITP)_2$ samples with SSAs of 556, 641 and 732 m^2 g^{-1} (Supplementary Fig. 20). Scanning electron micrographs demonstrate that the sample with the highest SSA has larger rod-like crystallites in the MOF powder (Supplementary Fig. 21), indicating enhanced crystallinity[8,35,36], as verified by the powder X-ray diffraction patterns of the samples with different SSAs (Supplementary Fig. 22).

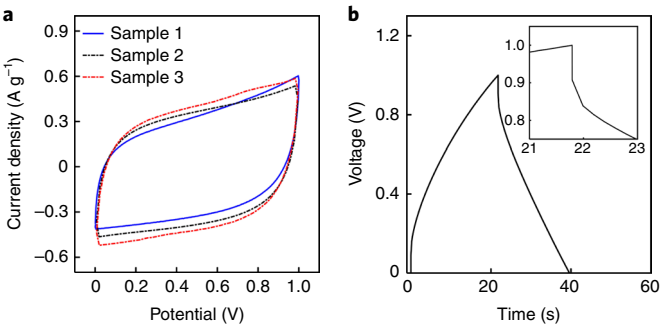

Fig. 5 | Electrochemical measurement of $Ni_3(HITP)_2$ electrodes in a symmetrical supercapacitor cell. a, Cyclic voltammograms at a scan rate of 10 mV s^{-1}. Samples 1, 2 and 3 have SSAs of 556, 641 and 732 m^2 g^{-1}, respectively. **b**, Galvanostatic charge and discharge curve of two-electrode cells with pellet MOF at a current density of 0.5 A g^{-1}. Inset: how to determine the ESR from the potential drop at the beginning of a constant current discharge.

Two-electrode cells were fabricated, with these $Ni_3(HITP)_2$ samples of different crystallinities, to measure the capacitance of this MOF in the RTIL [EMIM][BF_4] (for details see Methods). With cyclic voltammogram measurements at a scan rate of 10 mV s^{-1} (Fig. 5a; for results at 5 mV s^{-1} see Supplementary Fig. 23), we obtained that the gravimetric capacitances for $Ni_3(HITP)_2$, with SSAs of 556, 641 and 732 m^2 g^{-1}, are, respectively, 58, 70 and 76 F g^{-1}, which are all smaller than the MD-obtained capacitance of ~101 F g^{-1} with an SSA of 1,153 m^2 g^{-1}. This difference could be ascribed to the different SSAs resulting from the imperfect crystallinity (Supplementary Figs. 21 and 22). The areal capacitance, however, depends little on the SSA (~11 μF cm^{-2}, Supplementary Table 5), and is close to the modelling value of ~9 μF cm^{-2}. This weakly crystallinity-dependent areal capacitance of MOF electrodes suggests that pores accessible to ions contribute equally to charge storage, which is essentially different from typical porous carbons with pores of different sizes and shapes. Accordingly, by improving the MOF crystallinity, one could achieve both larger SSA and higher gravimetric capacitance, closer to the modelling value.

The up-to-date conductive MOFs, however, have smaller electrochemical voltage windows (limited by the onset of electrochemical reactions under positive and negative polarizations) than those achieved for metallic electrodes with RTILs[5–8,10,13,14]. Our cyclic voltammogram measurements of $Ni_3(HITP)_2$ in a three-electrode cell indicate that enhancing MOF crystallinity, accompanied by an SSA increase from 556 to 732 m^2 g^{-1}, would also enlarge its voltage window from about 2.1 to 2.8 V (Supplementary Fig. 24). Our cycle-life tests further confirm the increased working voltage with improving crystallinity (Supplementary Fig. 25).

We then measured the ESR of MOF-based EDLCs. The galvanostatic charge–discharge curve in Fig. 5b was experimentally obtained at room temperature for two-electrode cells composed of a 25-μm separator and $Ni_3(HITP)_2$ MOF pellets with 180 μm thickness and 6.4 mm diameter. The ESR was found to be 8.6 Ω cm^2, similar to our electrochemical impedance spectroscopy (EIS) data (8.9 Ω cm^2, Supplementary Fig. 26). Previous experiments have reported a smaller ESR of this MOF than of porous carbons in organic electrolyte[10]. To identify this advantage of $Ni_3(HITP)_2$ in RTIL electrolyte, a commercial activated carbon (YP-50F) was chosen for comparison, with nearly the same size and mass loading and without any binders and additives. The ESR for the assembled cells with [EMIM][BF_4] was determined from galvanostatic

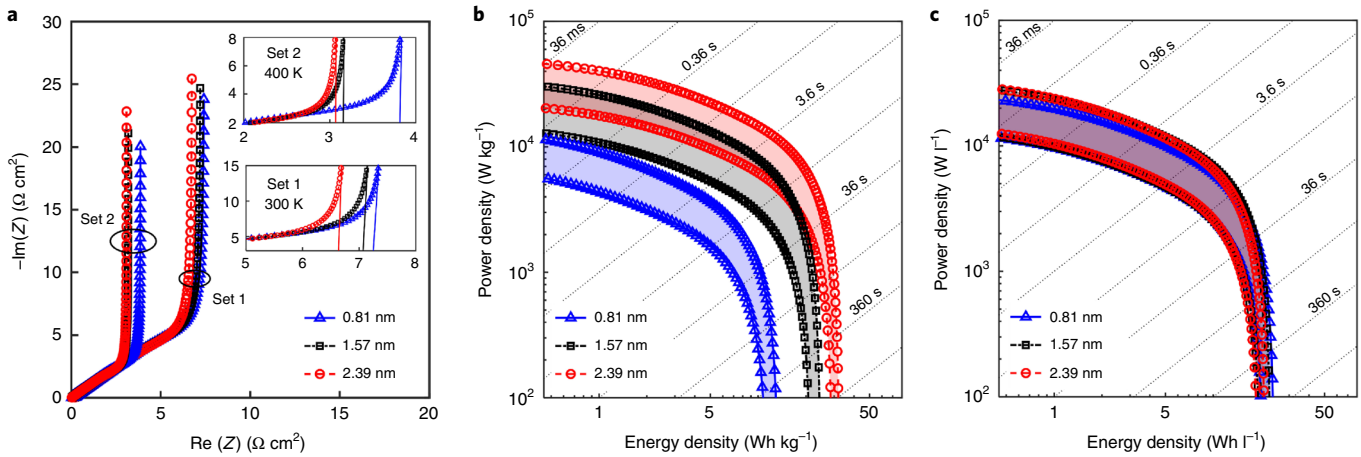

Fig. 6 | Capacitive performance predicted for practical cell-size supercapacitors. a, Nyquist plots for MOF-based supercapacitors at temperatures of 300 K and 400 K. **b**,**c**, Gravimetric (**b**) and volumetric (**c**) Ragone plots for MOF-based supercapacitors from 300 to 400 K. Straight grey, dotted lines in **b** and **c** indicate the lasting time, which quantifies how long a supercapacitor can supply the power at an appointed power–energy point. The voltage between the cathode and anode is 2.8 V.

charge–discharge curves as about 7.2 and 15.9 Ω cm^2, respectively, for electrodes made of $Ni_3(HITP)_2$ and activated carbon with Ni foam collectors (Supplementary Fig. 27). It was earlier experimentally demonstrated that electrodes based on aligned single-walled carbon nanotubes show greatly enhanced ion transport parallel to the alignment direction[37]. Similarly, the MOFs studied herein, possessing crystal structure and retaining crystallinity when made into electrodes[10,32], could offer straight quasicylindrical pores, providing faster charging dynamics than the carbon with tortuous pores and amorphous topology.

The MD-obtained capacitance and conductivity of electrolyte in an MOF pore, together with intrinsic properties of MOFs (Supplementary Table 2), could be used to assess the capacitive performance of a practical MOF-based supercapacitor, via macroscale equivalent circuit simulations (Supplementary Fig. 28; for details see Methods and Supplementary Section 8). On the basis of the values of σ and capacitance, for the three studied MOFs, Nyquist plots were computed for supercapacitors with the same-sized MOF electrode (180 μm thickness and 6.4 mm diameter) and separator (25 μm thickness). They differ, to some extent, from EIS measurements (Fig. 6a versus Supplementary Fig. 26), as modelling adopts ideal monocrystalline MOF electrodes and neglects the electrode and electrode–collector contact resistances. From simulation-obtained Nyquist plots, ESRs of such cells at 400 K were found to be 3.1, 2.9 and 2.3 Ω cm^2 for MOFs with pore sizes of 0.81, 1.57 and 2.39 nm, respectively. At 300 K, ESR increases to approximately 6.4 Ω cm^2 for the three MOF electrodes (Fig. 6b), which is compatible with our experimental values from both galvanostatic charge–discharge and EIS measurements. These results indicate that the ESR of MOF-electrode EDLCs is dominated by the resistances of the in-pore electrolytes. Therefore, molecular modelling is quite an appropriate approach to assessing both charge storage and charging dynamics of MOF supercapacitors at the macroscale.

Ragone plots for the temperature-dependent power–energy relationships and the lasting times of MOF supercapacitors are shown in Fig. 6b,c. The temperature shows a minor influence on maximal energy density but has a large effect on the power density. For applications demanding the best gravimetric performance, MOFs with the largest pore size (2.39 nm) seem to be a better choice, delivering both higher energy and higher power density, in comparison with the other two MOFs (Fig. 6b). As the temperature increases from 300 to 400 K, under a cell voltage of 2.8 V, the MOF with the largest pore size could reach a power density of 20–46 kW kg^{-1} and an energy density of about 30 Wh kg^{-1}. For optimized volumetric performance, all three MOFs exhibit similar promising performance, with a power density range of 13–30 kW l^{-1} and energy density of ~20 Wh l^{-1}. These compare favourably with the performance of most reported carbon-based EDLCs (Supplementary Table 6)[22–24,38,39]. As expected, under higher voltages, the energy and power densities would both increase (Supplementary Fig. 29).

Conclusion

We have investigated the charge storage and charging dynamics of supercapacitors consisting of conductive MOF electrodes and RTIL electrolyte. The microstructures of RTIL inside MOF pores were analysed in terms of in-plane (2D) and axial (1D) ion distributions, as well as ion orientations, which help to interpret the obtained double-humped and bell shapes of the capacitance–potential dependence. With the TLM rationalizing the charging dynamics, we evaluated the capacitive performance of macroscale EDLC devices. Modelling results revealed that these MOF/RTIL-based cells could exhibit performance superior to most carbon-based devices[22–24,38,39], which suggests promising avenues for designing supercapacitors with both high energy and high power densities.

The improvement of MOF crystallinity obtained through different synthesis procedures was shown to enlarge not only the SSA and particle size[8,35,36] but also the working voltage. The electrochemical measurements on supercapacitors made of MOF materials solely as electrodes and RTILs as electrolytes have shown that the gravimetric capacitance increases with SSA. The ESR of the MOF supercapacitor is smaller than that of a similarly structured cell with a typical commercial porous carbon, showing the benefit of the well controlled monodisperse pore structures in MOFs. Both areal capacitance and resistance obtained in experiment agree with modelling, signifying that our molecular simulations could well represent the real MOF-based supercapacitor systems.

Although many conductive MOFs have been synthesized[5–8,40], they are still a new family in the MOF community and more of them need to be developed, which would take the modelling-guided design as key input. Moreover, to-be-developed 3D conductive MOF scaffolds might be expected to have advantages over the dense stacks of 2D MOF sheets with quasi-1D pores. Indeed, 3D scaffolds could provide ion transport paths in all directions and consequently promote cation–anion swapping, pivotal in charging–discharging processes. Such scaffold electrodes with all-dimension openness

and high porosity may help to enhance the charging dynamics, and together with the enhanced surface area potentially enlarge energy and power densities simultaneously.

Online content

Any methods, additional references, Nature Research reporting summaries, source data, extended data, supplementary information, acknowledgements, peer review information; details of author contributions and competing interests; and statements of data and code availability are available at https://doi.org/10.1038/s41563-019-0598-7.

Received: 16 February 2019; Accepted: 19 December 2019;
Published online: 03 February 2020

References

1. Simon, P. & Gogotsi, Y. Materials for electrochemical capacitors. *Nat. Mater.* **7**, 845–854 (2008).
2. Sun, H. et al. Hierarchical 3D electrodes for electrochemical energy storage. *Nat. Rev. Mater.* **4**, 45–60 (2018).
3. Furukawa, H., Cordova, K. E., O'Keeffe, M. & Yaghi, O. M. The chemistry and applications of metal-organic frameworks. *Science* **341**, 1230444 (2013).
4. Guan, B. Y., Yu, X. Y., Wu, H. B. & Lou, X. W. Complex nanostructures from materials based on metal–organic frameworks for electrochemical energy storage and conversion. *Adv. Mater.* **29**, 1703614 (2017).
5. Wang, H., Zhu, Q.-L., Zou, R. & Xu, Q. Metal-organic frameworks for energy applications. *Chem* **2**, 52–80 (2017).
6. Sun, L., Campbell, M. G. & Dincă, M. Electrically conductive porous metal–organic frameworks. *Angew. Chem. Int. Ed.* **55**, 3566–3579 (2016).
7. Zhou, J. & Wang, B. Emerging crystalline porous materials as a multifunctional platform for electrochemical energy storage. *Chem. Soc. Rev.* **46**, 6927–6945 (2017).
8. Feng, D. et al. Robust and conductive two-dimensional metal–organic frameworks with exceptionally high volumetric and areal capacitance. *Nat. Energy* **3**, 30–36 (2018).
9. Choi, K. M. et al. Supercapacitors of nanocrystalline metal–organic frameworks. *ACS Nano* **8**, 7451–7457 (2014).
10. Sheberla, D. et al. Conductive MOF electrodes for stable supercapacitors with high areal capacitance. *Nat. Mater.* **16**, 220–224 (2017).
11. Fedorov, M. V. & Kornyshev, A. A. Ionic liquids at electrified interfaces. *Chem. Rev.* **114**, 2978–3036 (2014).
12. Hayes, R., Warr, G. G. & Atkin, R. Structure and nanostructure in ionic liquids. *Chem. Rev.* **115**, 6357–6426 (2015).
13. Watanabe, M. et al. Application of ionic liquids to energy storage and conversion materials and devices. *Chem. Rev.* **117**, 7190–7239 (2017).
14. Armand, M., Endres, F., MacFarlane, D. R., Ohno, H. & Scrosati, B. Ionic-liquid materials for the electrochemical challenges of the future. *Nat. Mater.* **8**, 621–629 (2009).
15. Salanne, M. et al. Efficient storage mechanisms for building better supercapacitors. *Nat. Energy* **1**, 16070 (2016).
16. Vatamanu, J., Borodin, O., Olguin, M., Yushin, G. & Bedrov, D. Charge storage at the nanoscale: understanding the trends from the molecular scale perspective. *J. Mater. Chem. A* **5**, 21049–21076 (2017).
17. Zhan, C. et al. Computational insights into materials and interfaces for capacitive energy storage. *Adv. Sci.* **4**, 1700059 (2017).
18. Shao, Y. et al. Design and mechanisms of asymmetric supercapacitors. *Chem. Rev.* **118**, 9233–9280 (2018).
19. Vatamanu, J., Borodin, O. & Smith, G. D. Molecular insights into the potential and temperature dependences of the differential capacitance of a room-temperature ionic liquid at graphite electrodes. *J. Am. Chem. Soc.* **132**, 14825–14833 (2010).
20. Kornyshev, A. A. & Qiao, R. Three-dimensional double layers. *J. Phys. Chem. C* **118**, 18285–18290 (2014).
21. Largeot, C. et al. Relation between the ion size and pore size for an electric double-layer capacitor. *J. Am. Chem. Soc.* **130**, 2730–2731 (2008).
22. Zhong, C. et al. A review of electrolyte materials and compositions for electrochemical supercapacitors. *Chem. Soc. Rev.* **44**, 7484–7539 (2015).
23. Yang, X., Cheng, C., Wang, Y., Qiu, L. & Li, D. Liquid-mediated dense integration of graphene materials for compact capacitive energy storage. *Science* **341**, 534–537 (2013).
24. Yang, H. et al. Graphene supercapacitor with both high power and energy density. *Nanotechnology* **28**, 445401 (2017).
25. Kondrat, S., Wu, P., Qiao, R. & Kornyshev, A. A. Accelerating charging dynamics in subnanometre pores. *Nat. Mater.* **13**, 387–393 (2014).
26. Masarapu, C., Zeng, H. F., Hung, K. H. & Wei, B. Effect of temperature on the capacitance of carbon nanotube supercapacitors. *ACS Nano* **3**, 2199–2206 (2009).
27. Fletcher, S. I. et al. The effects of temperature on the performance of electrochemical double layer capacitors. *J. Power Sources* **195**, 7484–7488 (2010).
28. Stoppa, A., Zech, O., Kunz, W. & Buchner, R. The conductivity of imidazolium-based ionic liquids from (−35 to 195) °C. A. Variation of cation's alkyl chain. *J. Chem. Eng. Data* **55**, 1768–1773 (2010).
29. Kondrat, S. & Kornyshev, A. A. Superionic state in double-layer capacitors with nanoporous electrodes. *J. Phys. Condens. Matter* **23**, 022201 (2011).
30. Futamura, R. et al. Partial breaking of the Coulombic ordering of ionic liquids confined in carbon nanopores. *Nat. Mater.* **16**, 1225 (2017).
31. Merlet, C. et al. On the molecular origin of supercapacitance in nanoporous carbon electrodes. *Nat. Mater.* **11**, 306–310 (2012).
32. Sheberla, D. et al. High electrical conductivity in Ni_3(2,3,6,7,10,11-hexaiminotriphenylene)$_2$, a semiconducting metal–organic graphene analogue. *J. Am. Chem. Soc.* **136**, 8859–8862 (2014).
33. Chaban, V. V., Voroshylova, I. V. & Kalugin, O. N. A new force field model for the simulation of transport properties of imidazolium-based ionic liquids. *Phys. Chem. Chem. Phys.* **13**, 7910–7920 (2011).
34. Sun, L. et al. A microporous and naturally nanostructured thermoelectric metal-organic framework with ultralow thermal conductivity. *Joule* **1**, 168–177 (2017).
35. Park, J. et al. Stabilization of hexaaminobenzene in a 2D conductive metal–organic framework for high power sodium storage. *J. Am. Chem. Soc.* **140**, 10315–10323 (2018).
36. Nonoguchi, Y., Sato, D. & Kawai, T. Crystallinity-dependent thermoelectric properties of a two-dimensional coordination polymer: Ni_3(2,3,6,7,10,11-hexaiminotriphenylene)$_2$. *Polymers* **10**, 962 (2018).
37. Izadi-Najafabadi, A., Futaba, D. N., Iijima, S. & Hata, K. Ion diffusion and electrochemical capacitance in aligned and packed single-walled carbon nanotubes. *J. Am. Chem. Soc.* **132**, 18017–18019 (2010).
38. Eftekhari, A. Supercapacitors utilising ionic liquids. *Energy Storage Mater.* **9**, 47–69 (2017).
39. González, A., Goikolea, E., Barrena, J. A. & Mysyk, R. Review on supercapacitors: technologies and materials. *Renew. Sustain. Energy Rev.* **58**, 1189–1206 (2016).
40. Li, P. & Wang, B. Recent development and application of conductive MOFs. *Isr. J. Chem.* **58**, 1010–1018 (2018).

Methods

MD simulation. As shown in Fig. 1, the MD simulation system consists of two identical and symmetric conductive MOFs immersed in an [EMIM][BF_4] RTIL. Real supercapacitors contain an electronically isolating ion transport membrane that warrants the absence of a short cut between the electrodes; however, ideal membranes must not impede ion exchange between the electrodes. For this proof-of-principle study, considering therefore the best performance possible, we will not incorporate the membrane into our simulation cell. This strategy is generally adopted for MD modelling of supercapacitors[15,17,25,31,41]. The atomistic structures of $Ni_3(HITP)_2$ MOF were obtained from experimental measurements[32], and Ni_3(hexahydroxybenzene)$_2$ ($Ni_3(HHB)_2$) and Ni_3(2,3,8,9,14,15-hexaimino-trinaphthalene)$_2$ ($Ni_3(HITN)_2$) were MOFs constructed, respectively, with reference to $Cu_3(HHB)_2$ (ref. [42]) and $Ni_3(HITP)_2$. The geometry optimization of each MOF in Fig. 1c and the partial charge distribution for each MOF in the unpolarized state (Supplementary Fig. 1) were derived from density functional theory calculations, using the Vienna ab initio simulation package (VASP)[43]. Furthermore, the corresponding density of states was computed to demonstrate that all the MOFs studied are conductive (Supplementary Fig. 2), though $Ni_3(HHB)_2$ and $Ni_3(HITN)_2$ have not yet been successfully synthesized. Details of MOF structure optimization of MOFs and pore size calculation can be seen in Supplementary Section 1 and Supplementary Tables 1 and 2. The Lennard-Jones parameters for the MOF atoms were taken from the generic universal force field[44]; the coarse-grained model, which could provide the proper thermodynamic and dynamic properties, was adopted for [EMIM][BF_4] (ref. [31]). The simulation cells were chosen large enough to reproduce the bulk state in the central region of the RTIL reservoir connected with two electrodes, and periodic boundary conditions were applied in all directions. Specific system parameters are given in Supplementary Table 3.

Simulations were performed in the *NVT* ensemble using the customized MD software GROMACS[45]. The applied electrical potential between the two electrodes in Fig. 1 was maintained by the constant-potential method, as it allows the fluctuations of charges on electrode atoms during the simulation[15,31,41]. Details of the constant-potential method can be found in Supplementary Section 2 and Supplementary Fig. 3. To guarantee accuracy, the electrode charges are updated on the fly at every simulation step (2 fs). The electrolyte temperature was maintained at 400 K using the V-rescale thermostat[46]. The electrostatic interactions were computed using the particle mesh Ewald method[47]. A fast Fourier transform grid spacing of 0.1 nm and cubic interpolation for charge distribution were used to compute the electrostatic interactions in reciprocal space. A cutoff length of 1.2 nm was used in the direct summation of the non-electrostatic interactions and electrostatic interactions in real space. For each conductive MOF, the MD system was annealed from 500 to 400 K over a period of 10 ns, following by running for another 40 ns to reach equilibrium under null electrode potential. To explore the charging dynamics, five independent runs were performed to smooth the charging process data. To obtain microstructure and capacitance, a simulation was performed for 60 ns to ensure reaching equilibrium under the applied potential ranging from 0 to 6 V, and then another 60 ns production in the equilibrium state was run for analysis.

In metallic electrodes, before the onset of electrochemical reactions, there are no limitations on accommodating or depleting electrons. Their capacitance is determined by their ability to accumulate the ionic charge from the electrolyte. In electrodes built from low-dimensional materials, such as graphene and its derivatives, accommodation of electrons has its own laws, which give rise to the quantum capacitance contribution[48–50]; when the electrode's quantum capacitance is much larger than the electrolytic capacitance, the total capacitance will be dominated by the ionic contribution[16,50]. Thick dense stacks of 2D MOF sheets, even those that deliver large pores, are not electronically low dimensional. Unless the concentration of charge carriers in them is as low as in wide-band-gap semiconductors, they are expected to perform like bulk porous metallic electrodes; our density functional theory calculations demonstrate that all MOFs studied here are good conductors (Supplementary Fig. 2), thus we focus on the ionic contribution.

The electrode potential was obtained as the potential difference between the electrode and the electrolyte reservoir and calibrated relative to the PZC of the electrode, and therefore the differential capacitance was calculated by taking derivatives of the MD-obtained surface charge density as a function of electrode potential (details can be seen in Supplementary Section 2 and Supplementary Fig. 4). The electrical conductivity of the bulk [EMIM][BF_4] was evaluated via the time integral of electrical current autocorrelation functions, $\sigma_{\mathrm{RTIL}} = \frac{1}{3V_{\mathrm{RTIL}}k_{\mathrm{B}}T}\int_0^\infty \langle \mathbf{J}(0)\cdot\mathbf{J}(t)\rangle\, dt$, in which V_{RTIL} is the system volume of the bulk RTIL and $\mathbf{J}(t)$ denotes the electrical current. $\mathbf{J}(t)$ is defined by $\mathbf{J} = \sum_{i=1}^{N} q_i\mathbf{v}_i$, where N is the total number of ions, and q_i and $\mathbf{v}_i(t)$ are the charge and velocity of the ith ion, respectively.

It is worth noting that static properties of EDLCs were studied at a temperature of 400 K, which is generally used for MD simulations, to obtain the ion structure and capacitance[25,31], while the charging dynamics was ascertained within a temperature range of 300–400 K due to the large impact of temperature on dynamic properties[26,27].

Equivalent electrical circuit simulation. We conceived a practical-size two-electrode symmetric cell (Supplementary Fig. 28a), based on our EDLC cell with $Ni_3(HITP)_2$ pellet electrodes in the experiment. Specifically, the diameter of the MOF electrode was set as 6.4 mm, and the electrode thickness was taken as 180 μm for the three studied MOFs in Fig. 1. The equivalent-circuit model of the conceptual two-electrode symmetric cell was based on the TLM, in which the resistors and the capacitors were calculated on the basis of the size of the cell and the MD-obtained specific capacitance and conductivity of ions inside the MOFs. The circuit simulations were performed via Simulink, in which impedance measurement and constant power load (via a boosting d.c.–d.c. converter block) tests were carried out respectively to obtain the Nyquist and Ragone plots for the three MOF-based EDLCs in practical cell size. Details can be seen in Supplementary Section 8 and Supplementary Fig. 28.

Materials for experiments. All the starting materials were purchased from commercial suppliers. Specifically, 2,3,6,7,10,11-hexaaminotriphenylene hexahydrochloride (HATP·6HCl) was purchased from Alfa; $NiCl_2{\cdot}6H_2O$ was purchased from Sigma-Aldrich; concentrated aqueous ammonia was purchased from TCI; ethanol and acetone were purchased from Sinopharm. The RTIL [EMIM][BF_4] was purchased from Aladdin. Starting materials were used without further purification unless otherwise noted. Activated carbon was purchased from Kuraray Chemical, and used to compare with the MOF electrode material.

Synthesis of MOFs. On the basis of synthesis strategies reported in the previous work[10,34], we obtained electrode materials of $Ni_3(HITP)_2$ with different SSAs of 556, 641 and 732 $m^2\,g^{-1}$ through three different procedures, which are given below.

Procedure I. A solution of 323 mg (1.36 mmol) of $NiCl_2{\cdot}6H_2O$ in 20 ml of water was added to a solution of 487 mg (0.91 mmol) of HATP·6HCl in 140 ml of water. Throughout this work, all the water used was deionized. Then 4.5 ml of concentrated aqueous ammonia (NH_4OH, 14.79 mol l^{-1}) was added to the mixture. The mixture was stirred in a flask under air bubbling for 1 h at 60 °C, then air bubbling was turned off and the mixture was stirred for an additional 2 h at 60 °C. The resulting black powder was isolated by centrifugation immediately and washed with water (twice, 180 ml) and ethanol (twice, 180 ml). The solid was then dried under vacuum for 12 h at 150 °C. The product was kept in a refrigerator.

Procedure II. A solution of 162.1 mg (0.675 mmol) of $NiCl_2{\cdot}6H_2O$ in 10 ml of water was added to a solution of 243.7 mg (0.453 mmol) of HATP·6HCl in 70 ml of water. Then 2.25 ml of NH_4OH (14.79 mol l^{-1}) was added to the mixture. The mixture was stirred in a flask under air bubbling for 1 h at 60 °C, then air bubbling was turned off and the mixture was stirred for an additional 2 h at 60 °C. The resulting suspension was cooled in air for 1.5 h. The resulting black powder was isolated by centrifugation and washed with water (twice, 90 ml) and ethanol (twice, 90 ml). The solid was then dried under vacuum for 8 h at 100 °C. After cooling, it was dried under vacuum for an additional 12 h at 100 °C. The product was kept in an argon-filled glovebox.

Procedure III. A solution of 96.5 mg (0.406 mmol) of $NiCl_2{\cdot}6H_2O$ in 10 ml of water was added to a solution of 142.0 mg (0.264 mmol) of HATP·6HCl in 50 ml of water in a 250-ml Schlenk bottle. The resulting yellow solution was stirred manually, heated to 65 °C in an oil bath and treated with 1.5 ml of NH_4OH (14.79 mol l^{-1}). The reaction mixture was kept at 65 °C for 45 min under continuous air bubbling then switched to a N_2 atmosphere and kept at 65 °C for an additional 2 h. The resulting suspension was cooled in a N_2 atmosphere for 2 h. The resulting black powder was separated from the reaction mixture by centrifugation, soaked in water at room temperature for 18 h and washed with water (twice,180 ml), ethanol (twice, 180 ml) and acetone (twice, 180 ml). Finally, the solid product was dried under a stream of nitrogen gas for 12 h. The product was kept in an argon-filled glovebox.

Characterization of MOF powder. Nitrogen adsorption–desorption isotherms were measured with a Quantachrome Autosorb IQ system at 77 K. Before the gas adsorption–desorption measurement, as-synthesized MOF (~100-mg) samples were activated by drying under vacuum for 12 h at 100 °C. Afterwards, liquid nitrogen baths (77 K) were used to measure nitrogen adsorption–desorption isotherms. The free-space correction and measurement were conducted using ultrahigh-purity grade (99.999% purity) nitrogen and helium, oil-free valves and gas regulators. Powder X-ray direction patterns were obtained with a PANalytical Empyrean X-ray powder diffractometer equipped with a Cu-sealed tube ($\lambda = 1.544426$ Å) at 40 kV and 40 mA, and samples were prepared on a zero-background silicon crystal plate. Scanning electron microscopy observation was performed with a Zeiss Gemini 300 scanning electron microscope with an operating voltage of 3 kV. Transmission electron microscopy was performed on a FEI Tecnai G2 F20 microscope and operated at 300 kV (point resolution 80 pm). Samples for transmission electron microscopy were dispersed in acetone, and a droplet of the suspension was transferred onto a carbon-coated copper grid.

Electrochemical measurement and analysis. A two-electrode cell was fabricated to measure the capacitive performance of MOF electrodes in an argon-filled glovebox. Before electrochemical measurement, the electrolyte [EMIM][BF_4] was vacuum-dried for 12 h at 100 °C and then treated with ultrapure argon (99.999%) to remove absorbed water and dissolved gas as much as possible. The cell is assumed to be symmetric, since the difference between the MOF materials in the

two electrodes was controlled to within 5%. All electrochemical measurements were performed on a Zahner Zennium electrochemical workstation.

Throughout this work, all the MOF electrodes were fabricated without any binders or conductive additives. To measure the capacitance, MOF powders were compressed into a Ni foam working electrode with a mass loading of ~4 mg cm^{-2}. We calculated the C_g of one single electrode from the cyclic voltammetry curves, according to the following equation:

$$C_g = 4\frac{\int_0^{V_0/\nu} I\,dt}{V_0 m} \quad (3)$$

where I and ν are the discharge current and the scan rate, respectively, V_0 is the operating voltage and m is the total active material mass of both electrodes in the symmetric cell.

The experimental C_g can be compared with the MD-obtained integral capacitance (C_g^{MD}). C_g^{MD} can be obtained directly from the molecular simulation that is performed under V_0 potential drop between the two electrodes, as $C_g^{MD} = 4\frac{Q}{V_0 m}$, in which Q is the total charge on one electrode. To obtain the ESR, the electrode is made of MOF pellets with 6.4 mm diameter and 180 µm thickness (mass loading ~ 5.9 mg cm^{-2}). Through galvanostatic charge–discharge measurements, we computed the ESR from the voltage drop (V_{drop}) at the beginning of the discharge curve from ESR = (V_{drop}/2I).

Data availability

The theoretical and experimental data presented in this work are available from the corresponding authors on reasonable request.

References

41. Vatamanu, J., Vatamanu, M. & Bedrov, D. Non-faradaic energy storage by room temperature ionic liquids in nanoporous electrodes. *ACS Nano* **9**, 5999–6017 (2015).
42. Park, J. et al. Synthetic routes for a 2D semiconductive copper hexahydroxybenzene metal–organic framework. *J. Am. Chem. Soc.* **140**, 14533–14537 (2018).
43. Kresse, G. & Furthmüller, J. Efficiency of ab-initio total energy calculations for metals and semiconductors using a plane-wave basis set. *Comput. Mater. Sci.* **6**, 15–50 (1996).
44. Rappe, A. K., Casewit, C. J., Colwell, K. S., Goddard, W. A. & Skiff, W. M. UFF, a full periodic table force field for molecular mechanics and molecular dynamics simulations. *J. Am. Chem. Soc.* **114**, 10024–10035 (1992).
45. Hess, B., Kutzner, C., van der Spoel, D. & Lindahl, E. GROMACS 4: algorithms for highly efficient, load-balanced, and scalable molecular simulation. *J. Chem. Theory Comput.* **4**, 435–447 (2008).
46. Bussi, G., Donadio, D. & Parrinello, M. Canonical sampling through velocity rescaling. *J. Chem. Phys.* **126**, 014101 (2007).
47. Gingrich, T. R. & Wilson, M. On the Ewald summation of Gaussian charges for the simulation of metallic surfaces. *Chem. Phys. Lett.* **500**, 178–183 (2010).
48. Fang, T., Konar, A., Xing, H. & Jena, D. Carrier statistics and quantum capacitance of graphene sheets and ribbons. *Appl. Phys. Lett.* **91**, 092109–092103 (2007).
49. Xia, J., Chen, F., Li, J. & Tao, N. Measurement of the quantum capacitance of graphene. *Nat. Nanotechnol.* **4**, 505–509 (2009).
50. Zhan, C., Neal, J., Wu, J. & Jiang, D. Quantum effects on the capacitance of graphene-based electrodes. *J. Phys. Chem. C* **119**, 22297–22303 (2015).

Acknowledgements

G.F., S.B., Ming Chen, L.N., Mingyu Chen, T.W., J.W., R.W. and J.F. acknowledge the funding support from the National Natural Science Foundation of China (51876072, 51836003) and Shenzhen Basic Research Project (JCYJ20170307171511292). S.B. and R.W. thank the China Scholarship Council for financial support. A.A.K. acknowledges the Leverhulme Trust for funding (RPG-2016-223), HUST for the support of this project through the HUST Honorary Professorship, and Imperial College for the support of this form of collaboration between the involved HUST and Imperial groups, and thanks the Imperial College–MIT seed fund for supporting the collaboration between the two universities. M.D., H.B. and T.C. thank the Army Research Office (W911NF-17-1-0174) for support. The computation was completed using the Tianhe II supercomputer in the National Supercomputing Center in Guangzhou. Part of the characterization was performed at the Analytical & Testing Center of HUST.

Author contributions

G.F. and A.A.K. set the strategy of this project in consultation with M.D.; G.F. devised simulation approaches; G.F. and M.D. designed the experiment. S.B. performed the major part of the MD simulations with participation of Ming Chen, R.W. and J.F.; Ming Chen did all density functional theory calculations; H.B., L.N., Mingyu Chen, T.W., J.W. and T.C. carried out the experiment, in which L.N. developed MOF synthesis procedures; G.F., S.B., Ming Chen, L.N., Mingyu Chen and A.A.K. analysed the data and wrote the manuscript; G.F., S.B., A.A.K., Ming Chen, H.B. and M.D. contributed to the discussion of results, editing and revising the paper.

Competing interests

The authors declare no competing interests.

Additional information

Supplementary information is available for this paper at https://doi.org/10.1038/s41563-019-0598-7.

Correspondence and requests for materials should be addressed to A.A.K. or G.F.

Reprints and permissions information is available at www.nature.com/reprints.